







Article

Study of a New Novel HVOAF Coating Based on a New Multicomponent Al80Mg10Si5Cu5 Alloy

Ester Villanueva ^{1,*}, Iban Vicario ¹, Carlos Vaquero ¹, Joseba Albizuri ², Maria Teresa Guraya ², Nerea Burgos ³ and Iñaki Hurtado ⁴

- ¹ Metal Processing Platform, TECNALIA Research & Innovation, Basque Research and Technology Alliance (BRTA), E48160 Derio, Spain; iban.vicario@tecnalia.com (I.V.); carlos.vaquero@tecnalia.com (C.V.)
² Department of Mechanical Engineering and Metallurgy, University of the Basque Country (UPV/EHU), E48013 Bilbao, Spain; joseba.albizuri@ehu.eus (J.A.); teresa.guraya@ehu.eus (M.T.G.)
³ Division of Materials & Manufacturing, CEIT-IK4, Basque Research and Technology Alliance (BRTA), E20018 Donostia-San Sebastian, Spain; nburgos@ceit.es
⁴ Mechanical and Manufacturing Department, Mondragon University, E20500 Arrasate-Mondragon, Spain; ihurtado@mondragon.edu
* Correspondence: ester.villanueva@tecnalia.com

Abstract: This paper presents and demonstrates the development of a new lightweight coating for aluminum alloy from a novel multicomponent alloy based on the AlSiMgCu system. The coating was applied using a newly designed approach that combined high velocity oxy-fuel (HVOF) and plasma spraying processes. This hybrid technique enables the deposition of coatings with enhanced performance characteristics. The optical microscopy (OM) and scanning electron microscopy with energy dispersive X-ray spectroscopy (SEM + EDS) revealed a strong adhesion and compaction between the multicomponent coating and the A6061 substrate. The new coating improved hardness by 50% and increased electrical conductivity by approximately 3.3 times compared to the as-cast alloy. Corrosion tests showed a lower corrosion rate, comparable to thermally treated A6061 alloy. Tribological tests indicated over 20% reduction in friction and over 50% reduction in wear rate. This suggests that multicomponent aluminum coatings could improve automotive and parts in contact with hydrogen by enhancing hydrogen fragilization resistance, corrosion resistance, electrical conductivity, and wear properties, with further optimization of thermal spraying potentially boosting performance even further.

Keywords: coating; plasma; HVOF; multicomponent aluminum alloy; wear; electrical conductivity; hardness; microstructure



Citation: Villanueva, E.; Vicario, I.; Vaquero, C.; Albizuri, J.; Guraya, M.T.; Burgos, N.; Hurtado, I. Study of a New Novel HVOAF Coating Based on a New Multicomponent Al80Mg10Si5Cu5 Alloy. *Coatings* **2024**, *14*, 1135. <https://doi.org/10.3390/coatings14091135>

Academic Editors: Nadia Arrousse and Hamza Ichou

Received: 5 August 2024

Revised: 29 August 2024

Accepted: 2 September 2024

Published: 4 September 2024



Copyright: © 2024 by the authors. Licensee MDPI, Basel, Switzerland. This article is an open access article distributed under the terms and conditions of the Creative Commons Attribution (CC BY) license (<https://creativecommons.org/licenses/by/4.0/>).

1. Introduction

Protective coatings have proven a high effectivity in extending the lifespan of metallic structures and in multiple sectors, including automation parts, with the recent trend to employ aluminum instead of steel due to its fuel economy benefits [1]. These coatings include paints, organic and inorganic coatings, diffusion layers, metallic coatings, and galvanization [2]. Thermal spray is a highly versatile technology to obtain ceramic and metallic coatings suitable for various applications and components. It is effective against wear, corrosion, and harsh high-temperature environments, and it enhances thermal efficiency, such as through insulation in aluminum engine cylinders [3]. Additionally, it is ideal for the repair and restoration of components [4].

Within the thermal spray techniques, several processes are noteworthy, including cold spray [4], HVOF, twin wire arc spraying, powder or detonation flame spraying, atmospheric plasma spraying, and arc spraying [5]. These methods differ in their application techniques, such as the form of feedstock, material generation, transport medium velocity, transport medium temperature, and the unique properties they impart.

Among the advanced thermal spray techniques, HVOF technology stands out. This innovative method employs a combustion system with high-pressure fuel and oxidizer gases to induce a detonation within the combustion chamber. This process partially or fully melts the material, accelerating it to adhere effectively to the substrate. The result is a high-velocity fluid haze with temperatures reaching up to 3000 °C and supersonic speeds ranging between 400 and 1.000 m/s [6,7]. By optimizing parameters, such as the fuel and oxygen flow rate, powder feed rate [8], spray distance, and carrier gas flow rate, it is possible to produce compact coatings with excellent resistance to abrasion, heat, friction, and wear [9–11]. Notably, thermally sprayed coating with a thickness of just 1 mm can achieve hardness values up to 2000 HV [12].

Porosity, which influences corrosion alongside nanocrystalline amorphous phases and the hardness of the coating, will depend on the oxygen flow rate followed by the powder feed rate and spray distance [13]. The spray distance will also affect the phase degradation, deposition efficiency, and bonding strength [9]. Additionally, the angle of incidence impacts the final properties, with a higher preheating temperature and a lower angle of incidence enhancing the corrosion resistance of coatings [14]. Also, gun speed can be important in the final properties of the coating. Faster gun movement reduces torch dwell time, spraying less powder and lowering the coating temperature [15].

Compared to other thermal spray processes, HVOF coatings offer superior surface quality [13]. Additionally, when compared to other high-performance techniques such as atmospheric plasma spraying (APS), HVOF reduces the thermal degradation of the material [16].

Certain studies have reported the application of HVOF techniques on aluminum alloy substrates [17–22], using ceramic materials such as carbides and oxides as the primary coating material due to their high melting points. In some cases, carbides and oxides are combined with metals such as Co, Ni, and Cr to achieve a low oxygen content and excellent adhesion properties [23].

The application of a WC10Co4C coating on an aluminum substrate resulted in reduced mechanical properties [24]. Additionally, during friction tests, the carbide particles caused abrasion and fragmentation of the coating layers. The refinement of the microstructure, influenced by the feedstock powders, and the reduction of porosity led to an increase in hardness from 68 HV up to 920 HV in the Cr₃C₂ thermal spray coating on an Al-Si substrate [25]. Another study [26] demonstrated that an alumina coating up to 150 μm thick over an A6061 alloy resulted in hardness values ten times higher than the base. During the friction test, the substrate exhibited an abrasion wear mechanism with a secondary adhesion mechanism, causing severe plastic deformation and delamination, while the coating layer showed some cracks but no scratches or grooves, which are characteristics of abrasion wear. On AlZn5.5MgCu aluminum alloy, AlCuFe quasicrystal was deposited as a coating [27], showing friction coefficient values between 0.92 and 1.00. For A390 aluminum alloys, the Al₂O₃ coating showed lower adhesion and an unstable friction behavior, with a dynamic coefficient of friction of 0.8, compared to around 0.6 of the WC-based coating. Hardness values exceeded 1000 HV for WC-based coatings, while Al₂O₃-base coatings reached 315 HV. Abrasion and adhesion wear mechanisms were observed in all cases [28]. Combining Al₂O₃ with Y₂O₃ and TiO₂ in coatings has been reported to further enhance wear properties [29].

Some studies have explored aluminum-based coating on aluminum substrates, but there is limited information on the wear characteristics of ceramic and metallic coating on aluminum alloys, especially for automotive applications. A noteworthy article [30] discusses the use of a Ni-SiC-based composite on A356 aluminum alloy, which is commonly used in automobile cylinders and machine tool shafts. Under non-lubricating conditions, the friction coefficient averaged 0.55, and the wear rate ranged from $16 \times 10^{-4} \text{ mm}^3/\text{N}\cdot\text{m}$ to $39 \times 10^{-4} \text{ mm}^3/\text{N}\cdot\text{m}$. The wear mechanism involved both abrasion and delamination. In a lubricating environment, the coefficient of friction was reduced by a factor of 5, and the wear rate was 10 times lower compared to dry friction. The addition of sericite improved

the wear rate of 2024 aluminum alloy [31]; however, this alloy is primarily used in aircraft structures. Other alloys, such as titanium alloys (Ti6Al4V), have employed ceramic coatings such as TiC [32], which tripled wear resistance, although these alloys are mainly used in biological applications.

It has been demonstrated that metals such as aluminum are also beneficial for coating technologies, creating new demands for surface pre-treatment coatings for corrosion protection and paint adhesion in the automotive sector [33]. A notable recent development is the Alcoat project, which focuses on creating a new recycled aluminum coating for steel products [34].

A current trend and emerging opportunity that has garnered significant research attention over the past decade is the production of high entropy alloys (HEAs), also known as compositional complex alloys (CCAs) and multicomponent alloys [35]. The distinctiveness of these new alloys lies in their substantial improvement in mechanical properties. One of the fundamental concepts is to achieve a more disordered structure with five or more elements at or near equimolar composition, forming a solid solution phase, in contrast to conventional alloys, which are based on the central areas of phase diagrams [36]. Despite these new opportunities and their excellent mechanical properties [37,38], the large-scale production of Light High Entropy Alloys (LWHEAs) is limited, with vacuum die casting being the primary manufacturing process [39]. In some special cases, the investigated alloys include expensive elements such as Ag, which increases hardness and yield strength by more than 10% and elongation by 21% [40], or Nb [41]. However, the addition of these elements results in non-cost-effective alloys. Recently, it has been reported that rapid solidification processes can enhance the single-phase microstructures in these alloys with the absence of a dendritic microstructure [42], although, in some instances, this requirement is not met, resulting predominantly in intermetallic phases [43]. New studies have demonstrated that, despite the limited understanding of intermetallics in HEA alloys, they can act as very effective secondary phases [44].

The development of multi-component materials based on aluminum alloys holds promise. Aluminum matrix composite brake drums and rotors have been used in vehicles such as the Lotus Elise, Volkswagen Lupo 3L, Chrysler Plymouth Prowler, and General Motors EV-1 due to their thermal and wear properties [45].

The use of HVOF technology is limited due to economic reasons stemming from relatively expensive equipment and operational costs, particularly for raw material powders [46]. From this perspective, employing secondary aluminum alloys for thermal spray powders could yield cost-effective results.

In this research, a new thermal spray process combining HVOF and plasma technologies is employed. This new device utilizes a thermal plasma to enhance the combustion process within the HVOF spray torch and incorporates an auxiliary cold gas to assist in controlling the process temperature. The use of thermal plasma to assist combustion aims to increase the flexibility of the spray system in terms of operating parameters and the range of materials that can be sprayed [47].

As the raw material grain size influences the final mechanical properties, gas atomization has been selected as the method to convert a new multicomponent cast alloy into powder. This process provides grain sizes ranging from 10 μm to 150 μm [48]. Moreover, the alloy has been manufactured using the High-Pressure Die-Casting (HPDC) process, which also produces smaller grain sizes that are favorable for atomization [49].

It is noteworthy that due to oxidation, accelerated by process temperatures, these coatings can serve as effective thermal barrier coatings for components exposed to hot gases. This characteristic renders them suitable for transportation applications. One of the properties of some multicomponent alloys is the capability of avoiding hydrogen fragilization in metals, so they can also be interesting for hydrogen utilization [50,51].

2. Materials and Methods Experimental

2.1. Materials Substrate and Coating

A new multicomponent aluminum alloy based on the Al80Mg10Si5Cu5 system was used in the experimental study. This new alloy was obtained by the HPDC foundry process, involving high solidification speeds, and promotes microstructures with superior mechanical properties [52]. The initial as-cast condition phases included the aluminum matrix, primary and eutectic Mg₂Si particles of around 20 and 5 μm, respectively, and copper-rich phases (Al₂Cu and Al₂CuMg) with sizes around 10 μm.

The Al80Mg10Si5Cu5 alloy was converted into powder by gas atomization with a Leybold VIGA 2S atomizer (Leybold products, Cornellà de Llobregat, Spain) with Argon at a pressure of 2.4 MPa, and the melt temperature was set at 850 °C. Subsequently, a qualitative and semiquantitative analysis was performed by averaging the composition from three measurements, each covering over 100 particles. Figure 1 illustrates the irregular morphology of the powder obtained after atomization.

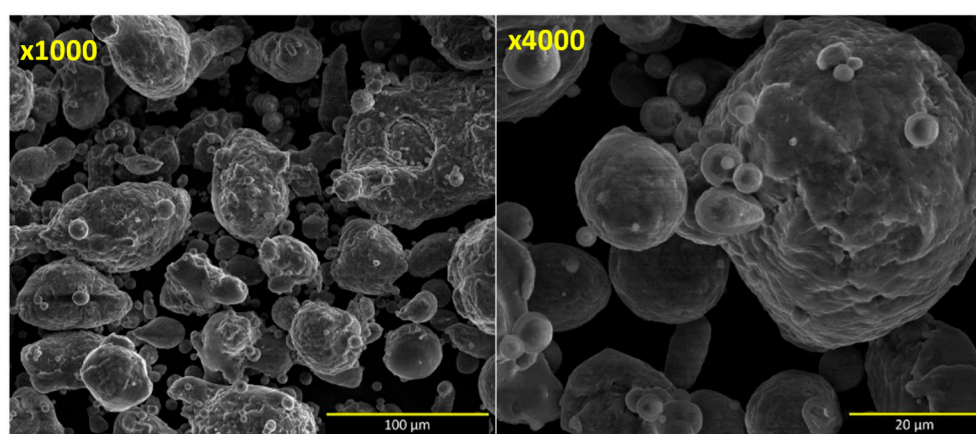


Figure 1. SEM image of the microstructure of Al80Mg10Si5Cu5 powder at ×1000 and ×4000 magnifications.

Finally, before the multicomponent material thermal spraying on the substrate, a sieving process was carried out with an optimum target size distribution between 63 and 250 μm in 4 runs.

As part of the material substrate, a commercially extruded A6061 aluminum alloy was employed. This alloy is commonly used in components for the automotive industry [53]. Commercial plates with dimensions of 40 mm × 30 mm and a thickness of 5 mm were used. Before the coating process, the samples were ground up to 800 grit with SiC paper, cleaned with propanol, and finally dried. Table 1 collects the chemical composition and Table 2 the mechanical, electrical, and thermal properties of the two experimental alloys.

Table 1. Chemical composition of experimental alloys in %wt.

Alloy	Al	Mg	Si	Cu	Mn	Fe	Zn
Al80Mg10Si5Cu5	78.9	10.3	5.6	4.7	0.1	0.3	0.1
A6061	98.2	0.9	-	0.9	-	-	-

Table 2. Mechanical, electrical, and thermal properties of experimental alloys.

Alloy	Hardness (HV3)	Electrical Conductivity (%IACS)	Melting Point (°C)
Al80Mg10Si5Cu5	130 ± 13.01	17 ± 0.55	592
A6061	68 ± 4.17	57 ± 0.41	585

2.2. Plasma Coating

A newly designed, self-manufactured system employing the HVOAF technology, a combination of HVOF and plasma, was employed to coat the prepared A6061 aluminum alloy. This system, named Kombus+, was engineered and produced by Tecnaia. The Kombus + system is based on a supersonic combustion projection system with oxygen and air. The mixture of gas + air/O₂ increases flows to maintain supersonic speed and pressure. Figure 2 illustrates the plasma equipment with the robot applying a coating to a sample.

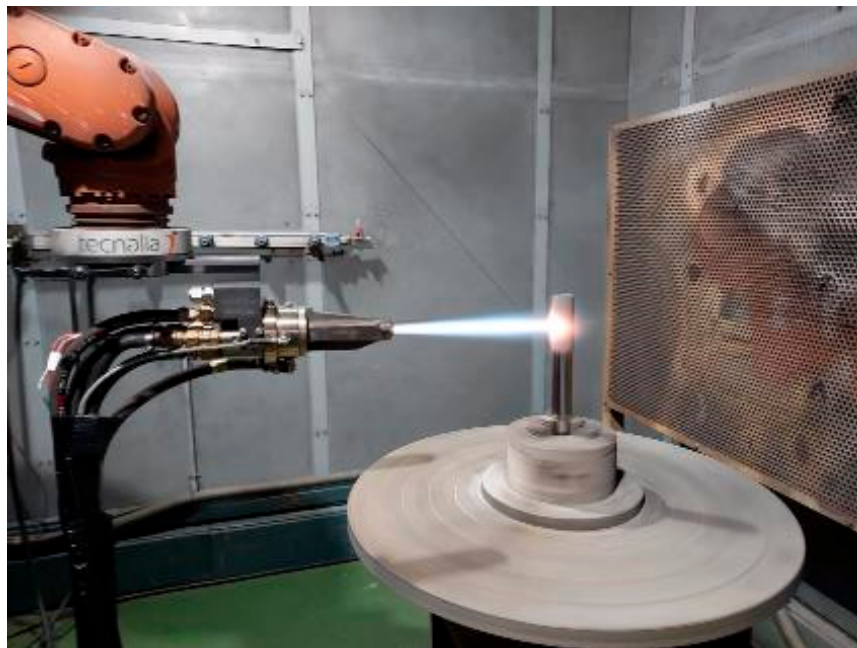


Figure 2. Plasma projecting with the robot.

The experimental parameters were specified: the fuel flow rate was calibrated to 380 L per min, with methane as the fuel gas because its maximum flame temperature [54] helped to reduce gas consumption and allowed the use of a fuel with a relatively low gross heating value [47].

The oxygen flow rate was set to 300 L per min, while the airflow was regulated at 1500 L per min with an air pressure of 14 bar. The carrier flow was adjusted to 90 liters per min, and the powder feed rate was set to 25% with a 90-degree incidence angle. The spray gun was positioned 300 mm from the substrate, moving at 0.9 m per second. The system operated at 250 revolutions per min.

These parameters have been selected based on accumulated experience [55–57] and as equipment manufacturers [58], which determined that they were the most optimal for aluminum alloys. They are considered ‘cold’ parameters due to the low melting point of the new multi-component aluminum alloy compared with other coating materials such as WC [59].

When measured with a pyrometer, the flame temperature reached 2000 °C while the substrate temperature was recorded at 200 °C.

2.3. Microstructural Analysis

The microstructure of the alloys was studied using a Leica DMI5000M optical microscope (LEICA, Wetzlar, Germany) and an EI Quanta 450 scanning electron microscopy (SEM) with Energy Dispersive Spectroscopy (EDX) analysis. The composition of the alloy produced by HPDC was determined using X-ray diffraction (XRD) with a Philips X’Pert Pro MPD PW3040/60 diffractometer (Malvern Panalytical Ltd., Malver, UK), equipped with a copper anode operating at 40 kV and 40 mA (1.6 kW). Scans were performed in a 2 θ range from 10° to 90°, with a step size of 0.02° 2 θ and a duration of 2 s per step. The X-ray

diffraction patterns were indexed with the PDF-2 database from the International Center for Diffraction Data (ICDD).

2.4. Hardness Study

Vickers indentations were employed to evaluate the hardness of the new material with the coating. The Vickers hardness was determined using a Vickers hardness tester model FV-700 (Mitutoyo, Kawasaki, Japan), selecting after several trials the load of 10 kgf as the best option. Measurements were taken at the top, bottom, and interface areas of the coating. Additionally, hardness measurements were taken on the substrate to ensure that the thermal process did not affect the mechanical properties of the base material. In total, 3 samples were analyzed.

2.5. Dry Sliding Wear Behavior

To investigate the tribological properties of the new coated aluminum alloy, dry sliding wear friction tests were conducted using a sphere-on-plate reciprocating configuration with a ball-on-disk (BOD) setup, following ASTM G99-05 standard without any lubricant. Tests were performed using a tribometer (MT2/60/NI/HT, Microtest S.A., Madrid, Spain). A total of 6 tests were performed: 3 tests on the coated material and another 3 on the substrate without the coating.

The testing parameters employed during the sliding wear friction tests are summarized in Table 3. The selection of these parameters aligns with tribological studies conducted on other high-wear performance aluminum alloys [60].

Table 3. Sliding wear test parameters.

Test Parameters	Selected Value
Load (N)	15.0
Velocity (m/s)	0.1
Rotation speed (rpm)	127.3
Sliding distance (m)	500.0
Track diameter (mm)	15
Environment	Dry air

Alumina balls with a diameter of 6 mm and hardness values ranging between 1250 and 1700 HV were used as counter-face bodies. The use of alumina spheres as a counterface ensures that the mechanically mixed layer (MML), which is common when steel balls are used and typically contains Al-Fe-O, is not formed. This minimizes chemically driven aspects of adhesive wear due to reduced chemical adhesion [61], thereby facilitating the determination of wear properties [62].

After completing the BOD tests, the determination of the wear coefficient rate was conducted using 3D laser scanning confocal microscopy (DCM 3D, Leica, Madrid, Spain). A total area of 20.8 mm × 20.2 mm and a height of 684 μm were measured using a 5X objective. At least 16 2D profiles were obtained using Leica map software version 3.2. Additionally, for comparison, four radii of 2.5 mm × 1.8 mm and a height of 275 μm were measured using the same 5X objective. The total volume loss was calculated, and wear coefficients were obtained in mm³/N·m [63,64].

Images of the wear track and cross-sections of the wear tracks were captured and analyzed to identify the wear mechanisms, using optical microscopy (OM), scanning electron microscopy (SEM), and confocal microscopy (CM).

2.6. Electrical Conductivity

The electrical conductivity (EC) was assessed with a portable conductivity meter, an Autosigma 3000 model (Jess W Jackson & Assoc., Buford, GA, USA). This device employs

the Eddy Current method to gauge conductivity and reports the results in the standard unit of %IACS (International Annealed Copper Standard). Conductivity measurements were performed on the newly coated material, with a minimum of five readings taken from the sample.

2.7. Corrosion Test

The general corrosion rate was determined using electrochemical techniques. Two different experiments, electrochemical impedance spectroscopy (EIS) and potentiodynamic polarization in the TAFEL region, were conducted on the new as-cast multicomponent Al80Mg10Si5Cu5 alloy. The combined use of these two techniques has been reported in some studies as an alternative to avoid practical issues that often reduce their reliability [65]. The tests were performed in a 3.5 wt.% sodium chloride solution. Before each test, the samples were grinded and stabilized for open circuit potential (OCP) for 60 min, adhering to ASTM G5 guidelines.

3. Results

3.1. Microstructure of New Al80Mg10Si5Cu5 Coating on A6061 Alloy

The XRD analysis of the new multicomponent alloy obtained by HPDC with high cooling rates is presented in Figure 3. As shown, the alloy exhibited four phases: an aluminum matrix, Mg₂Si, Al₂Cu, and Al₂CuMg.

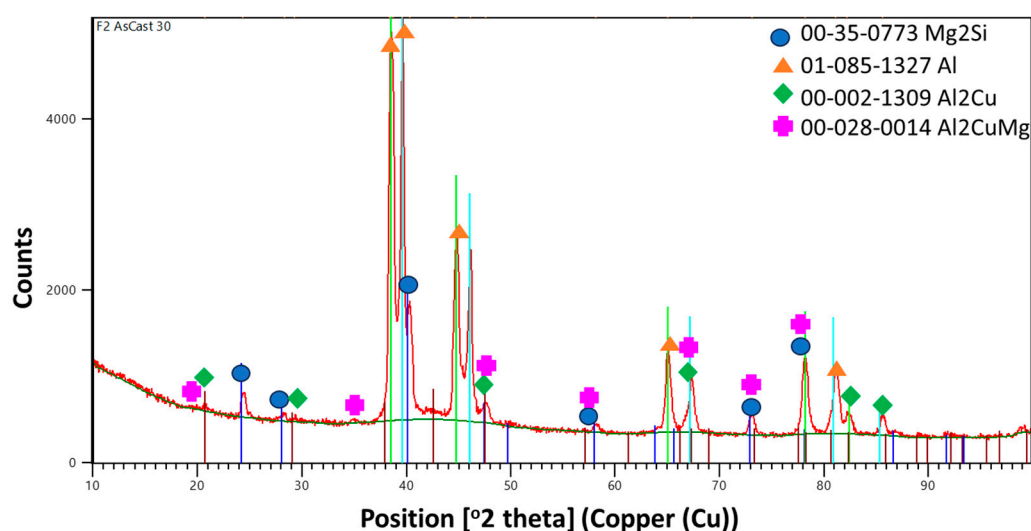


Figure 3. XRD analysis of Al80Mg10Si5Cu5 obtained by HPDC.

Following, Figure 4 shows the SEM images of the coated A6061 aluminum material with the Al80Mg10Si5Cu5 multicomponent alloy. Images revealed that the new coating achieved thicknesses ranging from 50 to 130 μm , though it was not completely homogeneous. The thickness of the developed coatings falls within the typical range obtained by thermal sprayed techniques (100–500 μm) [66], with the powder feed rate as the main parameter that influences the deposition rate, determining whether it is low or high [67].

EDS analysis, as presented in Table 4, indicated that while the new multicomponent alloy in its as-cast state exhibited four phases, the new coating displayed only two distinct phases. To confirm, the composition of each of the observed phases was analyzed and compared with literature data [68–70].

The primary phase corresponds to the aluminum matrix, appearing in gray (point 2). Light gray areas enriched with Mg, Si, and Cu (point 3) were observed and correlated with the aluminum matrix with Mg₂Si and part of Al₂Cu phases. Additionally, white-colored phases were correlated with Al₂CuMg phases with a splat pattern-like structure [29] at the grain boundaries of the aluminum matrix (point 4).

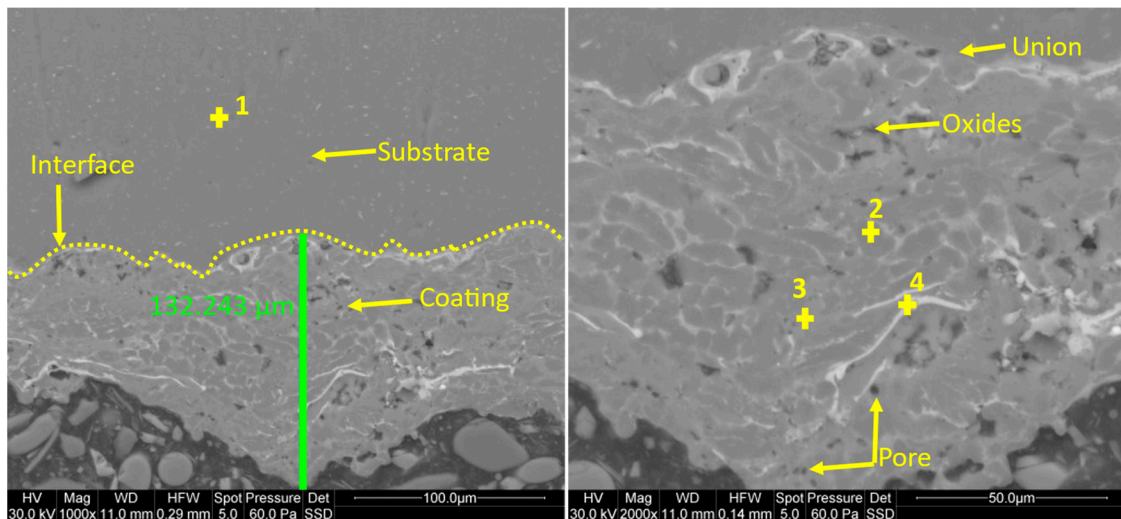


Figure 4. SEM micrographics of the new multicomponent-based coating at the magnification of $\times 1000$ and $\times 2000$.

Table 4. Chemical composition (wt.%) of new multicomponent-based coated material.

Point	Al	Mg	Si	Cu	Mn	Fe
1	97.14	1.0	-	1.30		0.6
2	82.8	7.9	5.5	3.6	0.4	
3	78.6	8.1	5.9	6.8	0.2	0.5
4	68.9	6.5	4.8	25.4		0.4

Due to the cooling and solidification rates of the HVOAF process, the interdiffusion of Cu and Al atoms leads to the dissolution of Al_2CuMg into the aluminum matrix [71]. As a result, the Al_2Cu phase was not observed in the new coated material, which instead formed the Al_2CuMg phase. This transformation has also been observed in previous studies [72,73], particularly when the alloy contains high magnesium levels and moderate amounts of copper following the homogenization treatment.

Moreover, the primary polygonal and eutectic globular Mg_2Si phases were fragmented and dispersed along grain boundaries [73]. It is noted that the dissolution of the Mg_2Si phase is much more rapid than the one of Al_2Cu and Al_2CuMg [74].

Additionally, because the HVOAF process was not performed in a protective atmosphere, some oxides were detected. Some of these oxides were elongated and parallel to the substrate, potentially resulting in a higher hardness in the new coating [75]. These oxides could also act as lubricants during the sliding process [76]. Spherical pores, appearing as black spots within the coating, were identified, especially at the bottom of the coating. Using ImageJ software version 1.54j, it was demonstrated that the porosity area was less than 2%, which is a low value compared to what is typically reported for thermal spray coatings [77]. These small pores in HVOF spraying are common due to shrinkage porosity [78]. According to the literature collected, porosity is affected by fuel flow rate, powder rate, and the spray distance [9,13,67].

As can be appreciated in the image, it was demonstrated that the HVOAF process resulted in good adhesion between the substrate and the coating [11]. This process eliminates the need for post-treatments typically required to enhance adhesive strength in other thermal methods [4].

By analyzing at higher magnifications ($\times 5000$) and applying an EDS line analysis (Figure 5) and a complementary EDS mapping for elemental analysis (Figure 6), the interface of the new coating was studied in more detail. The interface was especially enriched in copper, with aluminum, magnesium, and silicon as secondary elements, correlated with

the presence of the Al_2CuMg phase. The Al_2CuMg phase can serve as a crack initiation source [79]. However, its presence is advantageous in aluminum alloys [80] due to the higher strength and hardness values provided by the Al_2CuMg phase [81] compared to the Al_2Cu phase. Additionally, the deposition of this intermediate layer contributes to better adhesion of the coating to the substrate [25].

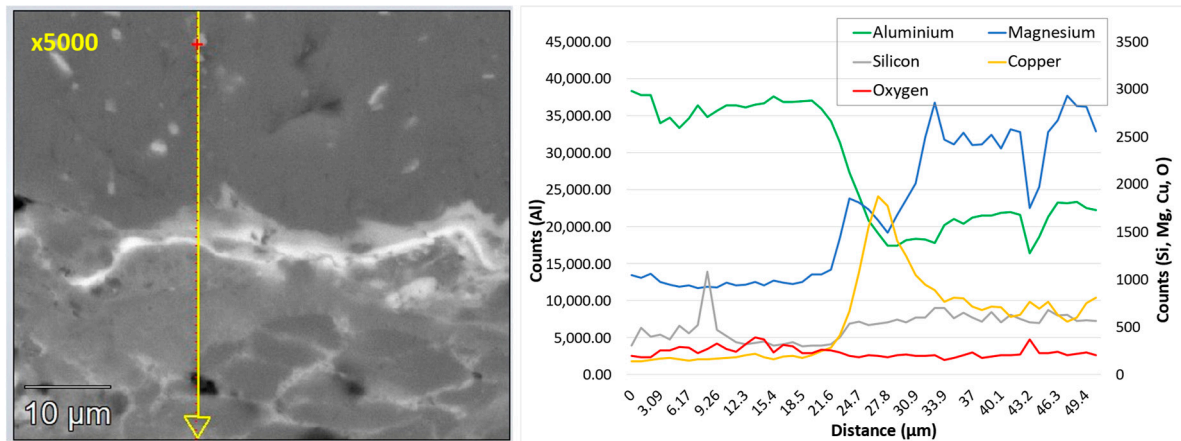


Figure 5. Line scan EDS analysis showing the distribution of each element across the different alloys and interfaces.

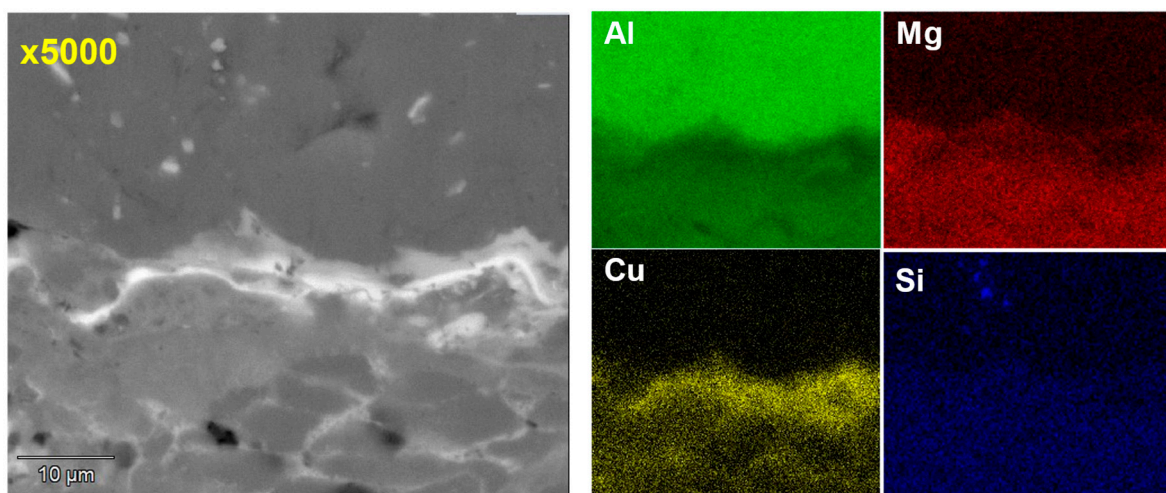


Figure 6. EDS map of element distribution in the alloys and interface.

3.2. Hardness

Figure 7 shows the optical micrograph with an example of indentations performed on the substrate, the interface, and the top and bottom of the coating, along with the graphic displaying the obtained mean results and standard deviation. The hardness track was smaller at the interface, resulting in a hardness of around 200 HV₁₀. This corroborated the microstructure analysis, which showed the Al_2CuMg phase precipitating at the interface, and this harder Al_2CuMg phase provides higher hardness values [81]. Notably, no cracks were identified at the interface after the indentations were performed, typical of fragile phases. By comparing the hardness of the coating with that of the substrate, it was demonstrated that the new multicomponent $\text{Al}_{180}\text{Mg}_{10}\text{Si}_5\text{Cu}_5$ aluminum-based coated material significantly improved the hardness of the A6061 alloy, achieving values of $133 \text{ HV}_{10} \pm 4.5$, which is two times higher. In addition, it was shown that the new coating provided a similar hardness value as the new multicomponent $\text{Al}_{180}\text{Mg}_{10}\text{Si}_5\text{Cu}_5$ alloy in its as-cast condition.

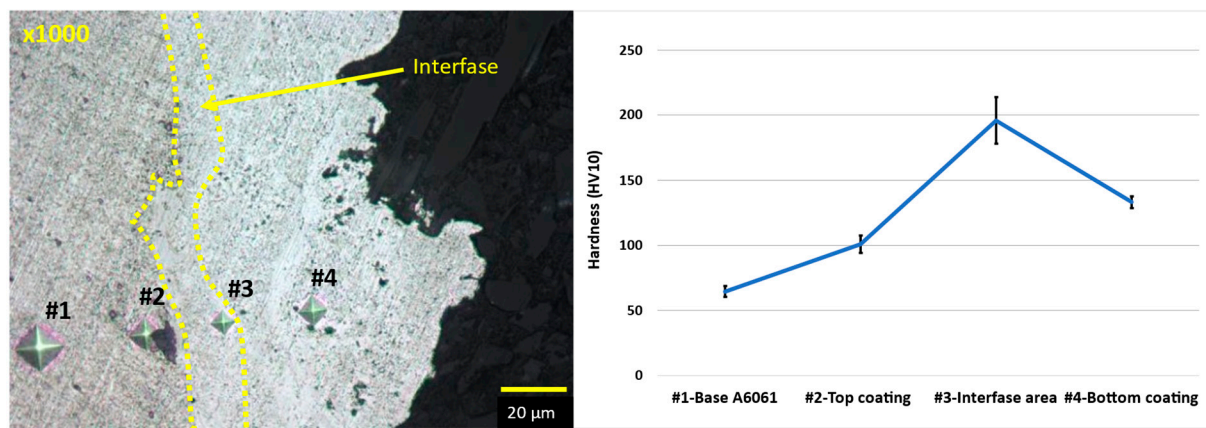


Figure 7. OM image showing indentations of a sample at the magnification of $\times 1000$ and hardness graph.

3.3. Tribological Properties

Figure 8 illustrates the evolution of the coefficient of friction (COF) values measured for the experimental samples: A6061 substrate alloy with the coating based on the multicomponent Al80Mg10Si5Cu5 alloy, A6061 substrate alloy without the coating, and the multicomponent Al80Mg10Si5Cu5 alloy in its as-cast state. Initially, during the first stages, the COF showed high values for the A6061 substrate without the coating and the multicomponent Al80Mg10Si5Cu5 alloy in its as-cast state, with a maximum COF exceeding 0.6. In contrast, the new coated material exhibited consistently lower values during the entire sliding test. Once the steady state was reached, both the multicomponent Al80Mg10Si5Cu5 alloy in its as-cast state and the A6061 alloy with the new coating showed COF with values around 0.4. On the other hand, the A6061 alloy without the coating maintained higher values, around 0.52, consistent with values reported in the literature for A6061 alloys [82]. The A6061 alloy without the coating also exhibited high fluctuations in the COF, attributed to particle fracture, periodic accumulation [83], and elimination of debris on the wear surface during dry sliding contact [84,85]. It was demonstrated that the new coating based on the multicomponent Al80Mg10Si5Cu5 alloy reduced friction by approximately 23%. Furthermore, the comparison with the hardness values confirmed that samples with higher hardness exhibited lower values for friction coefficient during the sliding process [86].

Figure 9 displays the 2D and 3D profiles of the wear tracks on the A6061 aluminum alloy with and without the coating based on the new multicomponent Al80Mg10Si5Cu5 alloy. The coated material exhibited a width of 1 mm and a maximum depth of 60 μm , whereas the uncoated material showed a width of 1.6 mm and a depth of 120 μm . It was demonstrated that the A6061 alloy coated with the new multicomponent Al80Mg10Si5Cu5 alloy had a reduced width and depth of the wear track compared to the A6061 substrate alloy without the coating.

In Table 5, COF mean values (μ) and deviations at the state stage and the wear rate coefficient (K) for each case are compiled. The A6061 alloy without the coating exhibited the highest values for the COF, corresponding to the highest wear rate observed among the samples. In contrast, the sample with the new coating showed a significantly reduced wear rate, approximately 0.4. The coating exhibited values corresponding to a moderate to severe wear regime, as documented in the literature for aluminum alloys, particularly for A6061 alloys [87,88]. These values are within the range reported for composite aluminum materials used in pistons, cylinders, engine blocks, brakes, and power transfer system elements [45].

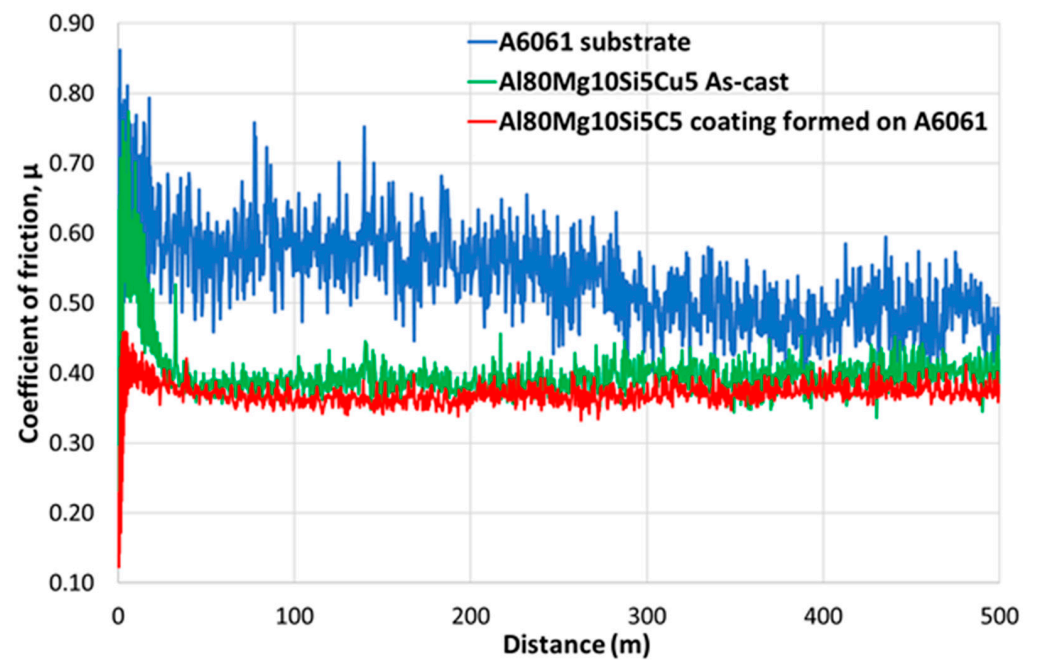


Figure 8. Evolution of the coefficient of friction for the experimental alloys: A6061 with and without the coating, and multicomponent Al80Mg10Si5Cu5 in as-cast state.

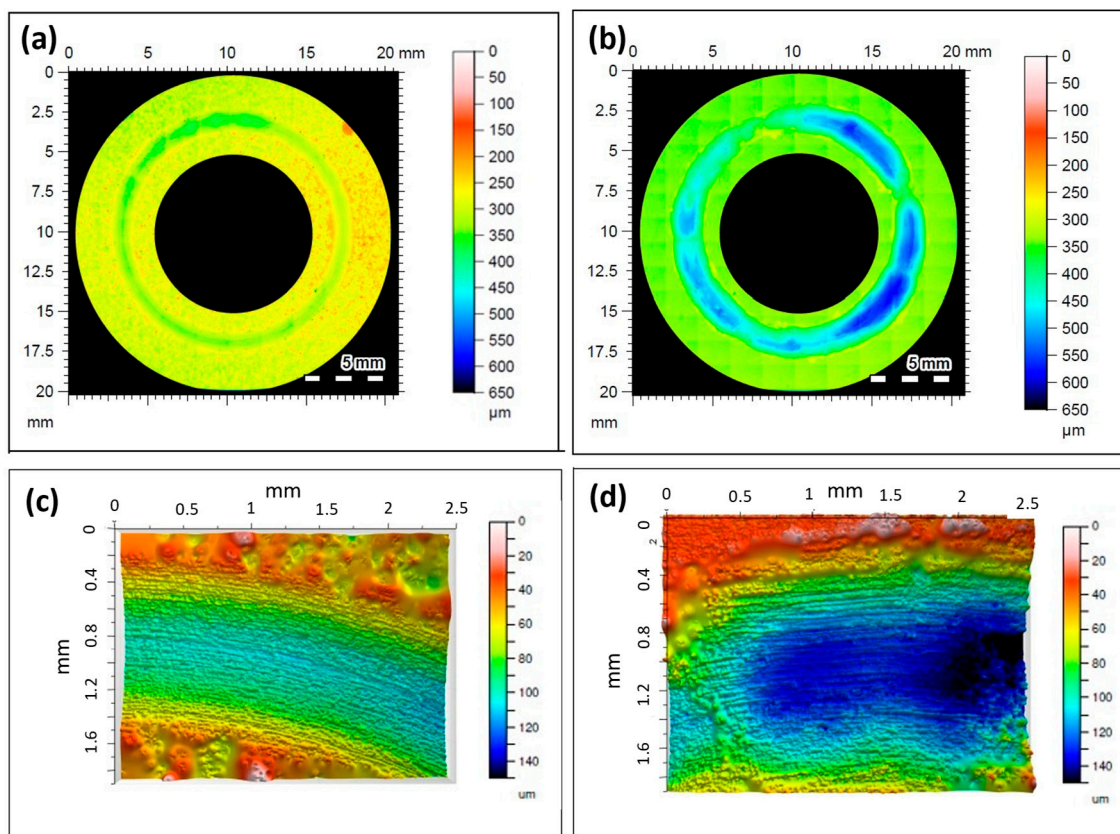


Figure 9. Wearing surface topographies. (a) 3D profile of A6061 with the coating; (b) 3D profile of A6061 without the coating; (c) 2D profile of A6061 with the coating; (d) 2D profile of A6061 without the coating.

Table 5. Friction (μ) and wear rate (K) coefficients.

Sample	μ	K ($\text{mm}^3/\text{N}\cdot\text{m}$)	Improvement μ (%)	Improvement K (%)
A6061 substrate	0.52 ± 0.05	$1.2 \times 10^{-3} \pm 0.000223$	-	-
As-cast Al80Mg10Si5Cu5	0.40 ± 0.04	$9.9 \times 10^{-4} \pm 0.000191$	23.08%	17.5%
A6061 with the Al80Mg10Si5Cu5 coating	0.40 ± 0.01	$5.3 \times 10^{-4} \pm 0.000019$	23.08%	55.83%

It is noteworthy that aluminum alloys could perform effectively under non-severe wear conditions, provided that delamination wear is effectively controlled [89].

To analyze the wear modes of the A6061 alloy with and without the coating based on the new multicomponent Al80Mg10Si5Cu5 alloy, the surfaces of the wear tracks were investigated as shown in Figure 10.

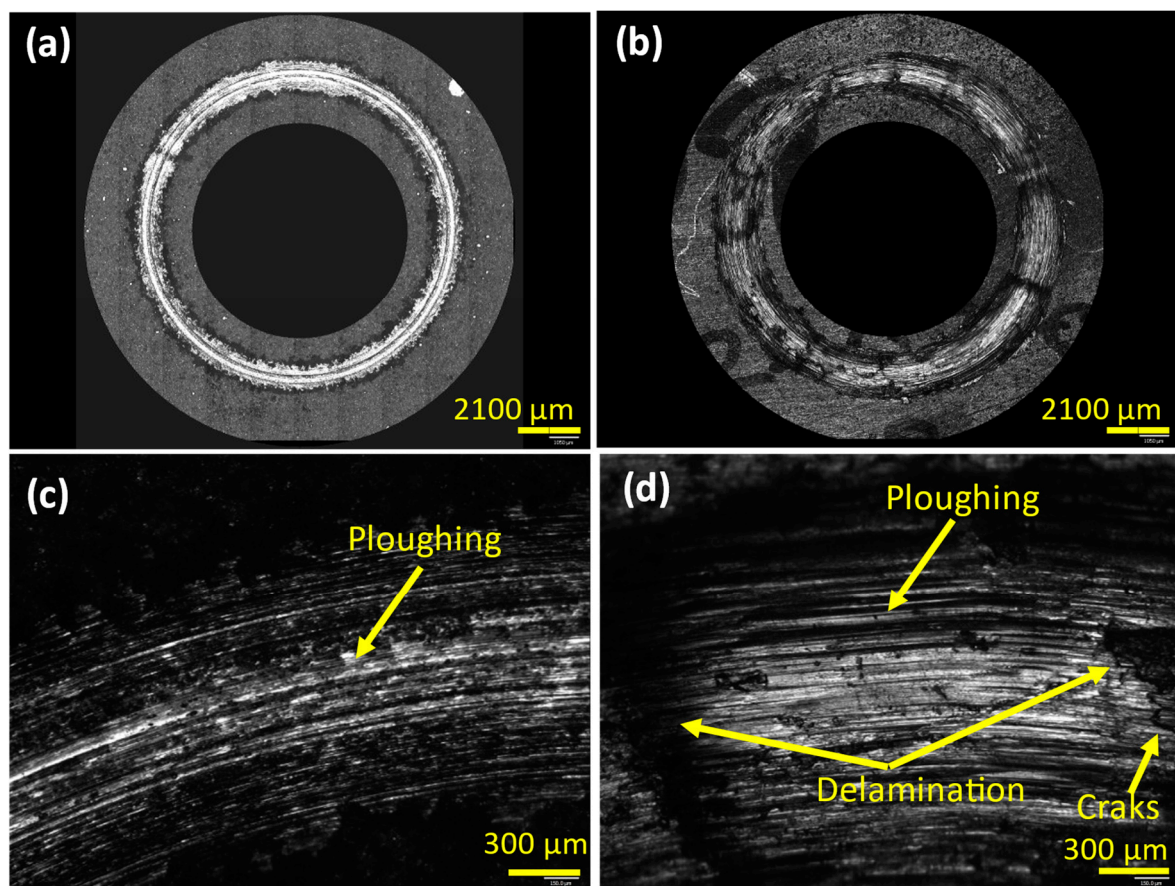


Figure 10. Laser confocal image of wear track at low magnification (a) A6061 with the coating, (b) A6061 without the coating at high magnification, (c) A6061 with the coating, and (d) A6061 without the coating.

The wear track of the coated A6061 alloy consisted of plowed areas, indicating an abrasion wear mechanism. In contrast, the A6061 alloy without the coating exhibited multiple wear mechanisms. In addition to plowed areas with wider scratches, some delaminated areas associated with cracks [90] were also visible on the wear track surface, indicating the presence of an adhesion mechanism [91–93]. The Al80Mg10Si5Cu5-based coating on the A6061 alloy exhibited a low friction coefficient, high hardness, and moderately low surface energy. These characteristics result in anti-adhesive properties [94], making the coated alloy superior to uncoated A6061, which has a higher friction coefficient and lower hardness.

The obtained results are consistent with those reported in the literature for the A6061 alloy, which is characterized by grooves and plowing due to abrasion and adhesion mechanisms [95,96], where delamination mode appears first as a substrate [97].

Figure 11 shows the cross-sectional microstructures of the A6061 alloy with and without the coating layer. It can be observed that after the sliding tests, the coating layer was still present on the coated A6061 alloy. Analyzing the samples with ImageJ software, it was determined that the highest thickness was around 60 μm , indicating that the coating had only worn by 40%. Additionally, no cracks were identified in the coating.

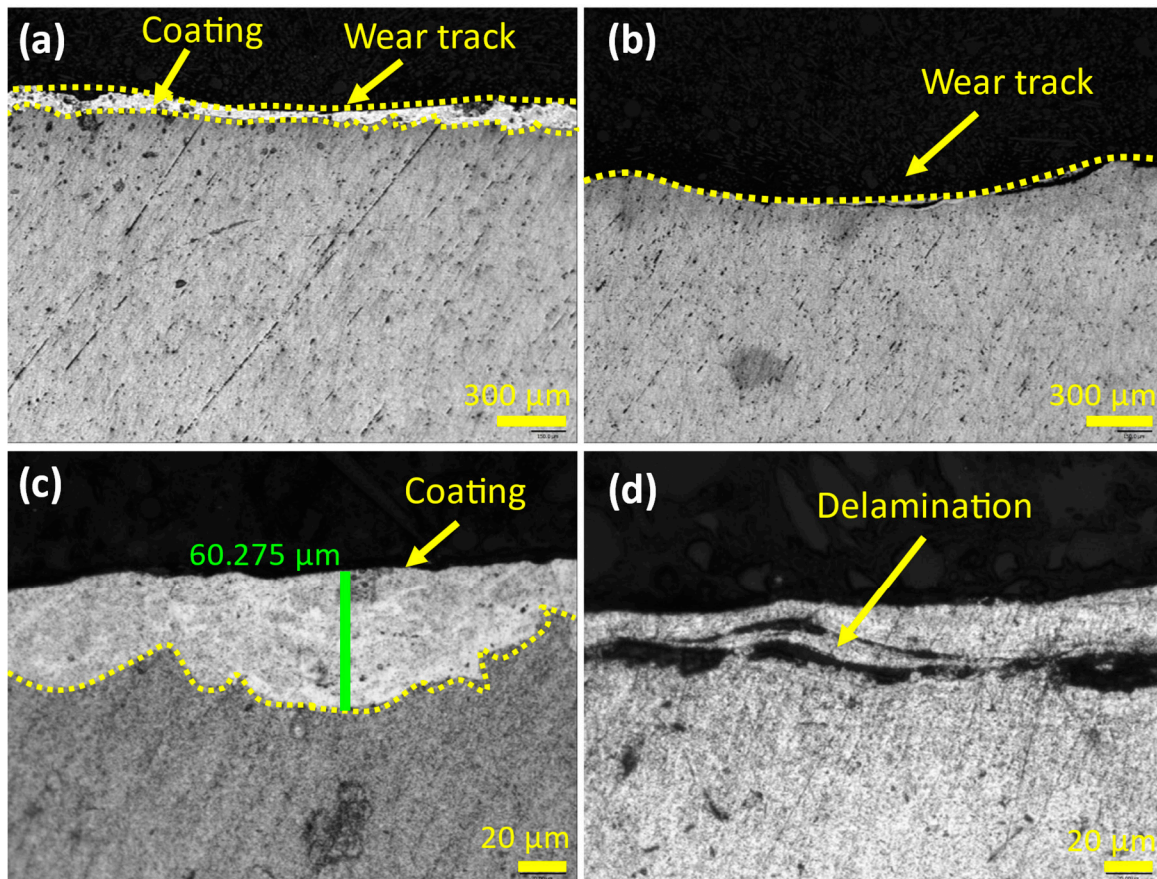


Figure 11. Laser confocal image of the cross-sectional microstructure, (a) A6061 with the coating at low magnification, (c) A6061 with the coating at high magnification, (b) A6061 without the coating at low magnification, and (d) A6061 without the coating at high magnification.

Consistent with the surface wear track analysis, the A6061 alloy without the coating exhibited delaminated areas on the subsurface [98] because of its lower hardness. The transition from mild to severe wear is marked by a shift from localized failure [99]. In conclusion, the surface and cross-sectional images of the wear track images agree with the wear rates and friction coefficient results discussed above.

3.4. Electrical Conductivity Characteristics

Table 6 collects the value for electrical conductivity obtained in the new multicomponent Al80Mg10Si5Cu5-based coated A6061 alloy. According to the results, the conductivity value obtained was slightly lower than that of pure aluminum (less than 10%) and very similar to that of the substrate A6061 alloy [100], as shown in Table 2. Additionally, the electrical conductivity of the coated material was 3.3 times higher than that of the Al80Mg10Si5Cu5 multicomponent alloy in its as-cast state, as shown in Table 2. This increase in conductivity is attributed to the thermal process and the high solidification rates involved in the coating process [101].

Table 6. Electrical conductivity (%IACS) of the new coated A6061 alloy.

Alloy	%IACS
A6061 with the Al80Mg10Si5Cu5 coating	56 ± 0.23

3.5. Corrosion Results

The parameters obtained through the tests conducted were the corrosion potential (E_{corr}) in volts, the corrosion current density (I_{cor}) in $\mu\text{A}/\text{cm}^2$, and the corrosion rate (Cor. Rate) in mm/year [102–104], which are presented in Tables 7 and 8.

Table 7. Results of corrosion of multicomponent Al80Mg10Si5Cu5 alloy, electrochemical impedance spectroscopy.

OCP (V)	R_s (Ω)	R_c (Ω)	R_p (Ω)	I_{cor} ($\mu\text{A}/\text{cm}^2$)	R_{cor} (mm/year)
−0.874	7.9	6909	31,890	0.681	0.007

Table 8. Results of corrosion of multicomponent Al80Mg10Si5Cu5 alloy, potentiodynamic polarization in the TAFEL region.

E_{cor} (V)	R_p (Ω)	I_{cor} ($\mu\text{A}/\text{cm}^2$)	R_{cor} (mm/year)
−0.743	154,600	0.118	0.001

By comparing the obtained values by both methods, the multicomponent Al80Mg10Si5Cu5 alloy employed as coating material showed lower corrosion resistance than those reported in the literature for conventional and multicomponent aluminum alloys [105]. High levels of silicon and copper typically contribute to poor corrosion resistance. However, in the new as-cast Al80Mg10Si5Cu5 alloy, the addition of a higher amount of copper compared to traditional aluminum alloys not only enhances hardness properties but also improves other material characteristics, such as the corrosion resistance.

When compared to the properties of the substrate A6061 alloy, the corrosion rate (mm/year) in the new multicomponent alloy was higher than in the Al6061 alloy, as documented in the literature [106,107]. Nevertheless, these values are like those presented for heat-treated A6061 alloy [108].

It is noticeable that the limited available and useful information for referencing different corrosion test methods complicates the comparison of obtained results [109–111].

3.6. Relation between Microstructure, Solidification Rate, and Electrical Conductivity

After analyzing the various obtained results, in this section, a study is conducted to investigate how the solidification temperature of the materials influences their microstructural properties, composition, and electrical conductivity. To provide a more comprehensive analysis, we have not only reviewed the experimental samples examined so far (as-cast Al80MgSi5Cu5 obtained by HPDC and Al80MgSi5Cu5-based coating produced by thermal spray) but also evaluated new samples solidified with different cooling rates: one from the Al80MgSi5Cu5 alloy solidified by gravity sand casting and another from the same alloy solidified in a metal die-cast, also using gravity.

Figure 12 illustrates the microstructures of the multicomponent Al80Mg10Si5Cu5 alloy as a function of different solidification rates [112–116], and Table 9 summarizes the chemical composition of each constituent in the multicomponent Al80Mg10Si5Cu alloy, based on the manufacturing process and cooling rate.

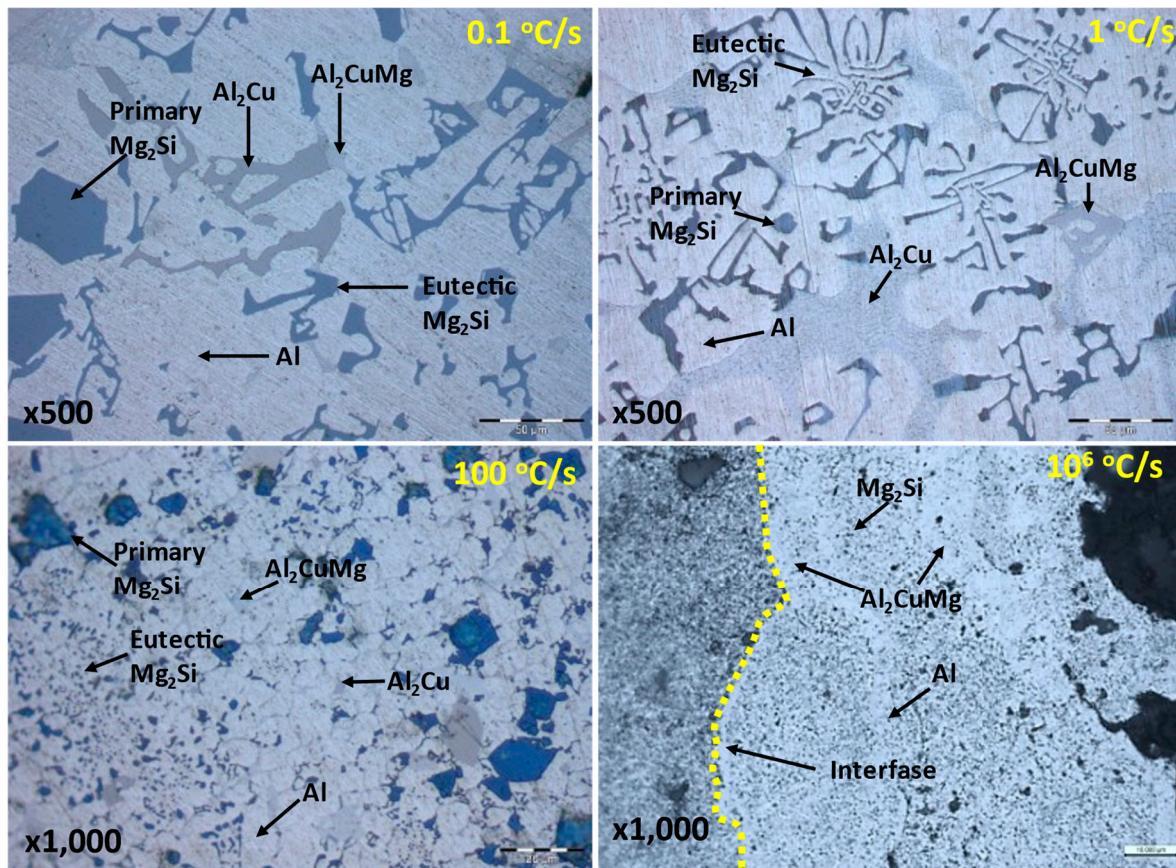


Figure 12. Comparison of microstructures in the Al80Mg10Si5Cu5 multicomponent alloy at different cooling rates.

Table 9. Approx. Chemical composition (wt.%) of phases contained in Al80Mg10Si5Cu alloy.

Phase	Gravity Sand	Gravity Die Cast	HPDC	Thermal Spray
Primary Mg ₂ Si	32Mg, 33Al, 34Si, 1Cu	34Mg, 31Al, 34Si, 1Cu	30Mg, 42Al, 25Si, 3Cu	-
Eutectic Mg ₂ Si	27Mg, 42Al, 29Si, 1Cu	28Mg, 41Al, 30Si, 1Cu	17Mg, 67Al, 14Si, 3Cu	-
Aluminum	93Al, 3Mg, 1Si, 2Cu	93Al, 4Mg, 1Si, 2Cu	88Al, 7Mg, 2Si, 3Cu	84Al, 8Mg, 6Si, 3Cu
Al ₂ Cu	66Al, 34Cu	66Al, 4Mg, 1Si, 29Cu	66Al, 8Mg, 1Si, 24Cu	-
Al ₂ CuMg	80Al, 15Mg, 1Si, 10Cu	75Al, 12Mg, 2Si, 11Cu	76Al, 11Mg, 2Si, 12Cu	76Al, 6Mg, 4Si, 15Cu

The sample solidified in a sand mold by gravity casting had the lowest cooling rate, approximately 0.1 °C/s. In this case, the aluminum matrix displayed polygonal Mg₂Si as the primary phase, eutectic Mg₂Si with a fine polygonal morphology, blocky Al₂Cu, and finally Al₂CuMg.

As the cooling rate increased during solidification in the gravity die cast (around 1 °C/s), some fine polygonal eutectic Mg₂Si transformed into a Chinese script-like structure. Additionally, the phases of Al₂Cu and Al₂CuMg displayed different morphology, with Al₂Cu appearing as lamellar and Al₂CuMg as blocky shapes [117], both solidifying particularly at the grain boundaries.

When the HPDC process was employed to obtain the Al80Mg10Si5Cu alloy with cooling rates exceeding 100 °C/s, the polygonal phases of Mg₂Si remained, but the eutectic Mg₂Si solidified with a globular shape and smaller particles. Both Al₂Cu and Al₂CuMg also appeared in smaller sizes and were located at the grain boundaries of the Al phase.

Finally, when the Al80Mg10Si5Cu5 alloy was produced by thermal spray with cooling rates around 10⁶ °C/s, small particles of Mg₂Si were dispersed throughout the matrix.

Additionally, the Al_2Cu phase was not detected, with only the presence of the Al_2CuMg phase precipitated in a splat pattern-like structure, particularly at the interfaces.

As shown in Figure 12, the morphology and copper content in the Mg_2Si and Al_2CuMg phases increased with the cooling rate, resulting in a supersaturated copper solution. It has been demonstrated that adding copper increases the electrical conductivity [118]. Also, it has been proved that altering the form, size, and morphology of the alloying elements enhances the conductivity of the alloy [119]. As a result, the microstructural transformations increase electrical conductivity [120–122].

Finally, Figure 13 correlates cooling rates with the corresponding morphology of the main constituents in Al80Mg10Si5Cu5 and its conductivity values. The results demonstrated that electrical conductivity is strongly influenced by both the cooling rate and the morphology of the constituents [123].

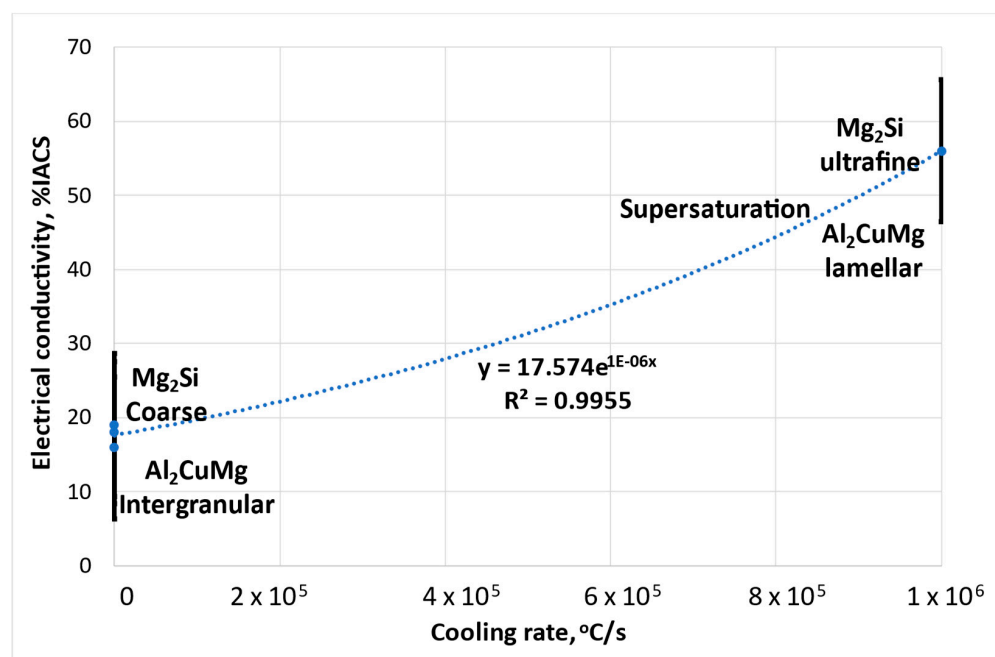


Figure 13. Correlation of %IACS with solution components and cooling rates.

4. Discussion

It has been demonstrated that using new multicomponent Al80Mg10Si5Cu5 aluminum alloys as a coating material for aluminum alloys improves mechanical, electrical, and tribological properties. Additionally, there was a slight improvement in corrosion resistance. The newly designed HVOAF process provided a high-quality coating with a thickness of up to $130\ \mu\text{m}$, though some pores were present at the bottom of the coating, accounting for less than 2% of the area. These pores are characteristic of this process. This thermal process requires experienced handling and optimization of parameters to achieve consistent coating quality. Parameters such as oxygen flow rate, spray distance, and powder feed rate can be optimized to improve porosity and coating thickness.

Microstructure and chemical analysis results indicated good adhesion between the substrate and the coating. The high solidification rates led to fewer phases and a finer microstructure, resulting in the disappearance of the Al_2Cu phase and the precipitation of Mg_2Si throughout the matrix. In the interface area, a high presence of elemental copper precipitated as the Al_2CuMg phase, providing high hardness without cracking.

Hardness results demonstrated a 50% increase in the new multicomponent-based coated material compared to the A6061 substrate alloy, reaching values up to 220 HV.

Tribological property results showed that the friction coefficient decreased by more than 20% in the new multicomponent alloy-based coated material compared to the A6061

substrate alloy, achieving a steady-state friction coefficient value of 0.40. This value was similar to that observed for the new multicomponent alloy in its as-cast state. Additionally, the wear coefficient decreased also significantly, being approximately 2.5 times lower than that of the uncoated sample.

The wear rate coefficient and the examination of the microstructure of the wear track surface and cross-sectional surface in the new coated material indicated mild wear conditions, characterized by abrasion as the principal wear mechanism. In contrast, the substrate without the coating exhibited moderate to severe wear, showing delaminated areas alongside ploughed areas attributed to a combination of abrasion and delamination mechanisms.

Comparing the hardness values of the experimental alloys revealed that samples with higher hardness demonstrated a lower COF during the sliding process. Additionally, it was observed that samples with significantly higher values for the coefficient of friction corresponded to the highest wear rate. However, it was noted that samples with a similar COF did not necessarily exhibit a linear relation with the wear rate.

The electrical conductivity results showed a significant increase ($\times 3$ times) compared to the multicomponent alloy in an as-cast state. The conductivity values approached those of the A6061 substrate and were comparable to a pure aluminum alloy. The analysis demonstrated a strong influence of the cooling rate and morphology of the constituents on electrical conductivity.

Corrosion resistance results demonstrated that the multicomponent alloy had higher values compared with other conventional and multicomponent aluminum alloys and were also higher than those of the heat-treated A6061 alloy. However, they were higher than the values for A6061 alloy in its as-cast state. Parameters such as preheating and angle of incidence should be investigated for a further increase in the corrosion resistance of the coating.

5. Conclusions

This study has explored the advanced properties of multicomponent alloys, clarified wear mechanisms, and showcased the benefits of a new thermal spray system for high-quality coatings.

A new coated material based on a new multicomponent aluminum alloy has been developed, featuring enhanced mechanical, electrical, and tribological properties.

Future work will focus on optimizing some thermal spray parameters to enhance specific properties. To achieve thicker coatings, a higher powder feeding rate will be investigated. Additionally, the angle of incidence and preheating will be optimized, as a lower angle of incidence and higher preheating have been shown to improve corrosion resistance.

Furthermore, the application of the Al80Mg10Si5Cu5 multicomponent alloy on the other types of aluminum substrates will be investigated. Extruded aluminum parts such as A5754 or A6060 and casting aluminum parts such as AlSi9Cu3 could benefit from increased electrical conductivity and improved wear properties. This presents a significant opportunity for the automotive industry, especially in developing electric vehicles and their batteries. It could lead to increased speed and greater load-bearing capacity.

Finally, studies are anticipated to evaluate these high-performance properties under real conditions and in casting parts, as well as the behavior against hydrogen fragilization.

Author Contributions: Conceptualization: E.V. and I.V.; methodology: C.V. and J.A.; validation: E.V., I.V., J.A., M.T.G., N.B., and I.H.; investigation: E.V., I.V., and J.A.; writing—original draft preparation: E.V., I.V., and J.A.; review and editing: M.T.G. and N.B.; supervision: I.V. and J.A.; project administration: E.V. and I.V.; funding acquisition: I.V. and J.A. All authors have read and agreed to the published version of the manuscript.

Funding: This work has been partially funded by the Basque Government through the ELKARTEK KK-2020_00047 (CEMAP), KK-2022_00082 (MINERVA), and KK-2023/00020 (DESGAS).

Institutional Review Board Statement: Not applicable.

Informed Consent Statement: Not applicable.

Data Availability Statement: Data is contained within the article.

Conflicts of Interest: The authors declare no conflicts of interest.

References

1. Tisza, M.; Czinege, I. Comparative study of the application of steels and aluminium in lightweight production of automotive parts. *Int. J. Lightweight Mater. Manuf.* **2018**, *1*, 229–238. [CrossRef]
2. Hanif, H.; Wang, T.; Su, L.; Li, H.; Zhu, Q.; Yang, A.; Li, Z.; Wang, W.; Zhu, H. In Situ Thermal Interactions of Cu-Based Anti-Corrosion Coatings on Steel Implemented by Surface Alloying. *Coating* **2024**, *14*, 722–739. [CrossRef]
3. Barbezat, G. Application of thermal spraying in the automobile industry. *Surf. Coat. Technol.* **2006**, *201*, 2028–2031. [CrossRef]
4. Sun, W.; Wei-Yee, A.; Wu, K.; Yin, S.; Yang, X.; Marinescu, I.; Liu, E. Post-Process Treatments on Supersonic Cold Sprayed Coatings: A Review. *Coatings* **2020**, *10*, 123. [CrossRef]
5. Gaur, U.; Kumari, E. Applications of Thermal Spray Coatings: A Review. *J. Therm. Spray Technol.* **2024**, *4*, 106–114. [CrossRef] [PubMed]
6. Bhatia, A. Thermal Spraying Technology and Applications. Course from the US Corps of Engineers, Publication EM 1110-2-3401. Available online: <https://www.cedengineering.com/userfiles/T04-002%20-%20Thermal%20Spraying%20Technology%20and%20Applications%20-%20US.pdf> (accessed on 4 August 2024).
7. Miguel, J.R.; Guilemany, J.M.; Carbonell, H. La Proyección Térmica de Alta Velocidad (HVOF) y Plasma: Qué Son y Para Qué Sirven. In Proceedings of the Conference: Jornadas sobre Tecnologías de Fabricación en la Industria, Ferrol, Spain, June 1997.
8. Sorour, A.; Adesina, A.Y.; Hussein, M.A.; Al-Daajani, B.F. Effect of Powder Feed Rate of Plasma-Sprayed Fe–Cr–Mo–B–C Coatings on Microstructure, Tribology and Corrosion in 3.5% NaCl Solution. *Arab. J. Sci. Eng.* **2022**, *47*, 7. [CrossRef]
9. Raza, A.; Ahmad, F.; Badri, T.M.; Raza, M.R.; Malik, K. An Influence of Oxygen Flow Rate and Spray Distance on the Porosity of HVOF Coating and Its Effects on Corrosion-A Review. *Materials* **2022**, *15*, 6329–6354. [CrossRef] [PubMed]
10. Taltavull, C.; López, A.J.; Torres, B.; Atrens, A.; Rams, J. Optimisation of the high velocity oxygen fuel (HVOF) parameters it is factible to produce effective corrosion control coatings on AZ91 magnesium alloy. *Mater. Corros.* **2014**, *66*, 423–433. [CrossRef]
11. Picas, J.A.; Rilla, A.F.; Martín, E. Mejora de la resistencia al desgaste de aleaciones de aluminio mediante recubrimientos obtenidos por proyección térmica HVOF. *Rev. Metal.* **2005**, *41*, 197–201. [CrossRef]
12. Recubrimientos Mediante Proyección Térmica: Comparativa Frente a Otras Tecnologías. Departamento Técnico de TMCOMAS 2016. Available online: <https://www.interempresas.net/TTS/Articulos/156162-Recubrimientos-mediante-proyeccion-termica-comparativa-frente-a-otras-tecnologias.html> (accessed on 4 August 2024).
13. Murugan, K.; Ragupathy, A.; Balasubramanian, V.; Sridhar, K. Optimizing HVOF spray process parameters to attain minimum porosity and maximum hardness in WC–10Co–4Cr coatings. *Surf. Coat. Technol.* **2014**, *247*, 90–102. [CrossRef]
14. Vanat, K.J.; Cortés, R.S.; Marendra, A.G. Microstructural Analysis of Aluminum Coatings Deposited by HVOF Process on Complex Surfaces. In Proceedings of the Conference: International Thermal Spray Conference—ITSC, Orlando, FL, USA, 7–10 May 2018. [CrossRef]
15. Pulido, N.; García, S.; Campo, M.; Rams, J.; Torres, B. Application of DOE and ANOVA in optimization of HVOF spraying parameters in the development of new Ti coatings. *J. Therm. Spray Technol.* **2020**, *29*, 4. [CrossRef]
16. Fernández, J.; Gaona, M.; Guilemany, J.M. La Proyección Térmica de Alta Velocidad (HVOF): Una Alternativa a la Proyección por Plasma de Hidroxiapatita. *Soc. Española Mater.* **2006**, *1*, 1109–1112.
17. Picas, J.A.; Rilla, A.F.; Martín, E. HVOF thermal sprayed coatings on aluminium alloys and aluminium matrix composites. *Surf. Coat. Technol.* **2005**, *200*, 1178–1181. [CrossRef]
18. Picas, J.A.; Menargues, S.; Martín, S.; Colominas, C.; Baile, M.T. Characterization of duplex coating system (HVOF + PVD) on light alloy substrates. *Surf. Coat. Technol.* **2016**, *318*, 326–331. [CrossRef]
19. HVOF Aluminum Bronze. Available online: <https://www.thermalspray.com/thermal-spray-coatings/spray-coating-materials/hvof-materials/hvof-aluminum-bronze/> (accessed on 4 August 2024).
20. Sobolev, V.V.; Guilemany, J.M.; Calero, J.A. Formation of structure of WC–Co coatings on aluminum alloy substrate during high-velocity oxygen-fuel (HVOF) spraying. *J. Therm. Spray Technol.* **1995**, *4*, 401–407. [CrossRef]
21. Pradeep, G.S.; Sunkad, S.; Jogeshwar, R.; Keshavamurthy, R.; Tambrallimath, V.; Jangam, S.; Basheer, D. Experimental Investigations on Erosion-Corrosion Characteristics of HVOF-Sprayed WC-10% Ni Coatings Deposited on Aluminum Alloy. *Adv. Mater. Sci. Eng.* **2023**, *1*, 8533871. [CrossRef]
22. Magnani, M.; Suegama, P.H.; Espallargas, N.; Fugivara, C.S.; Dosta, S.; Guilemany, J.M. Corrosion and Wear Studies of Cr3C2 2NiCr-HVOF Coatings Sprayed on AA7050 T7 under Cooling. *J. Therm. Spray Technol.* **2009**, *18*, 353–363. [CrossRef]
23. Moreira, F.; Ferreira, P.M.; Silva, R.J.C.; Santos, T.G.; Vidal, C. Aluminium-based dissimilar alloys surface composites reinforced with functional microparticles produced by upward friction stir processing. *Coating* **2023**, *13*, 962–980. [CrossRef]
24. Koutsomichalis, A.; Vardavoulis, M.; Vaxevanidis, N.M. HVOF sprayed WC–CoCr coatings on aluminum: Tensile and tribological properties. *OP Conf. Ser. Mater. Sci. Eng.* **2017**, *174*, 012062. [CrossRef]
25. Richert, M.; Ksiazek, M.; Leszczyńska-Madej, B.; Nejman, I.H.; Grzelka, R.; Palka, P. The Cr₃C₂ thermal spray coating on Al-Si substrate. *J. Achiev. Mater. Manuf. Eng.* **2010**, *38*, 95–102.

26. Ernesto, T.; Garza-Montes-de-Oca, N.F.; Pérez, A.; Hernandez-Rodriguez, M.A.L.; Hernández, A.J.; Colás, R. Wear of an aluminium alloy coated by plasma electrolytic oxidation. *Surf. Coat. Technol.* **2012**, *206*, 2213–2219. [[CrossRef](#)]
27. Torskaya, E.V.; Morozov, A.V.; Malyshev, V.N.; Shcherbakova, O.O. Processing and Tribological Properties of PEO Coatings on AlZn5.5MgCu Aluminium Alloy with Incorporated Al-Cu-Fe Quasicrystals. *Ceramics* **2023**, *6*, 858–871. [[CrossRef](#)]
28. Bang, J.; Lee, E. Enhancing wear resistance of A390 aluminium alloy: A comprehensive evaluation of Thermal Sprayed WC, CrC and Al₂O₃ coating. *Coatings* **2024**, *14*, 853. [[CrossRef](#)]
29. Medricky, J.; Lukac, F.; Csaki, S.; Houdkova, S.; Barbosa, M.; Tesar, T.; Cizek, J.; Musalek, R.; Kovarik, O.; Charska, T. Improvement of Mechanical Properties of Plasma Sprayed Al₂O₃-ZrO₂-SiO₂ Amorphous Coatings by Surface Crystallization. *Materials* **2019**, *12*, 3232. [[CrossRef](#)]
30. Huang, P.C.; Hou, K.H.; Hong, J.J.; Wang, G.L. Study of fabrication and wear properties of Ni-SiC composite coatings on A356 aluminum alloy. *Wear* **2021**, *477*, 203772. [[CrossRef](#)]
31. Xi, K.; Wu, H.; Zhou, C.; Qi, Z.; Yang, K.; Fu, R.; Xiao, S.; Wu, G.; Ding, K.; Chen, G.; et al. Improved corrosion and wear resistance of micro-arc oxidation coatings on the 2024 aluminum alloy by incorporation of quasi-two-dimensional sericite microplates. *Appl. Surf. Sci.* **2022**, *585*, 152693. [[CrossRef](#)]
32. Chen, T.; Deng, Z.; Liu, D.; Zhu, X.; Xiong, Y. Bioinert TiC ceramic coating prepared by laser cladding: Microstructures, wear resistance, and cytocompatibility of the coating. *Surf. Coat. Technol.* **2021**, *432*, 127635. [[CrossRef](#)]
33. Doerre, M.; Hibbitts, L.; Patrick, G.; Akafuah, N.K. Advances in Automotive Conversion Coatings during Pretreatment of the Body Structure: A Review. *Coatings* **2018**, *8*, 405. [[CrossRef](#)]
34. The Alcoat Project. Available online: <https://icn2.cat/en/news/5126-the-alcoat-project-will-enhance-steel-construction-safety-using-recycled-aluminium> (accessed on 4 August 2024).
35. Balaji, V.; Anthony, X. Development of high entropy alloys (HEAs): Current trends. *Heliyon* **2024**, *10*, e26464. [[CrossRef](#)]
36. Bilbao, Y.; Trujillo, J.J.; Vicario, I.; Arruebarrena, G.; Hurtado, I.; Guraya, T. X-ray Thermo-Diffraction Study of the Aluminum-Based Multicomponent Alloy Al₅₈Zn₂₈Si₈Mg₆. *Materials* **2022**, *15*, 5056. [[CrossRef](#)]
37. Yang, X.; Chen, S.; Cotton, J.D.; Zhang, Y. Phase stability of low-density, multiprincipal component alloys containing aluminium, magnesium, and lithium. *J. Miner. Met. Mater. Soc.* **2014**, *66*, 2009. [[CrossRef](#)]
38. Sanchez, J.M.; Vicario, I.; Albizuri, J.; Guraya, T.; Koval, N.E.; García, J.C. Compound formation and microstructure of As-cast high entropy aluminiums. *Metals* **2018**, *8*, 167. [[CrossRef](#)]
39. Kumar, A.; Gupta, M. An Insight into Evolution of Light Weight High Entropy Alloys: A Review. *Metals* **2016**, *6*, 199. [[CrossRef](#)]
40. Wang, Y.; Wu, X.; Cao, L.; Tong, X.; Zhu, Q.; Sonhbai, T.; Song, H.; Guo, M.X. Effect of Ag on aging precipitation behavior and mechanical properties of aluminum alloy 7075. *Mater. Sci. Eng. A* **2020**, *804*, 140515. [[CrossRef](#)]
41. Nwaeju, C.C.; Nnuka, E.E. Effect of niobium addition on the structure and mechanical properties of aluminum bronze. *Int. J. Res. Adv. Eng. Technol.* **2015**, *1*, 70–75.
42. Shao, Y.; Guo, P.; Liang, N.; Cheng, S.; Wang, J.; Xu, F. Microstructure refinement and enhanced mechanical properties in rapid-quenched MnCrFeCoNi high-entropy alloy. *Heliyon* **2023**, *9*, e22530. [[CrossRef](#)] [[PubMed](#)]
43. Liu, J.; Wang, X.; Singh, A.P.; Xu, H.; Kong, F.; Yang, F. The Evolution of Intermetallic Compounds in High-Entropy Alloys: From the Secondary Phase to the Main Phase. *Metals* **2021**, *11*, 2054. [[CrossRef](#)]
44. Tsai, M.H.; Tsai, R.C.; Chang, T.; Huang, W.F. Intermetallic Phases in High-Entropy Alloys: Statistical Analysis of their Prevalence and Structural Inheritance. *Metals* **2019**, *9*, 247. [[CrossRef](#)]
45. Vencl, A.; Rac, A.; Bobic, I. Tribological Behaviour of Al-Based MMCs and Their Application in Automotive Industry. *Tribol. Ind.* **2004**, *26*, 31–38.
46. Sarjas, H.; Goljandin, D.; Kulu, P.; Mikli, V.; Surzhenkov, A.; Vouristo, P. Wear Resistant Thermal Sprayed Composite Coatings Based on Iron Self-Fluxing Alloy and Recycled Cermet Powder. *Mater. Sci.* **2012**, *18*, 34–39. [[CrossRef](#)]
47. Martinez, B.; Mariaux, G.; Vardelle, A.M.; Barykin, G.; Parco, M. Numerical Investigation of a Hybrid HVOF-Plasma Spraying Process. *J. Therm. Spray Technol.* **2009**, *18*, 909–920. [[CrossRef](#)]
48. Descripción General de la Tecnología de Atomización de Metales. Available online: <https://met3dp.com/es/overview-of-metal-atomization-technology/> (accessed on 4 August 2024).
49. Jeon, M.; Lee, E. Effect of grain size on residual stress in AlSi10MnMg alloy. *JAMET* **2023**, *47*, 195–201. [[CrossRef](#)]
50. Luo, H.; Li, Z.; Raabe, D. Hydrogen enhances strength and ductility of an equiatomic high entropy alloy. *Sci. Rep.* **2017**, *7*, 9892. [[CrossRef](#)] [[PubMed](#)]
51. Luo, H.; Li, Z.; Lu, W.; Ponge, D.; Raabe, D. Hydrogen embrittlement of an interstitial equimolar high-entropy alloy. *Corros. Sci.* **2018**, *136*, 403–408. [[CrossRef](#)]
52. Tialong, Z.; Zhu, J.; Yang, T.; Luan, J.; Kong, H.L.; Liu, W.; Cao, B.; Wu, S.; Wang, D.; Wang, Y.; et al. A new $\alpha + \beta$ Ti-alloy with refined microstructures and enhanced mechanical properties in the as-cast state. *Scr. Mater.* **2022**, *207*, 114260. [[CrossRef](#)]
53. The Use of 6061 Aluminum Alloy in Cars. Available online: <http://www.autoaluminumsheet.com/a/the-use-of-6061-aluminum-alloy-in-cars.html> (accessed on 4 August 2024).
54. What Types of Gas Are Used in Thermal Spraying? Available online: <https://www.twi-global.com/technical-knowledge/faqs/faq-what-types-of-gas-are-used-in-thermal-spraying> (accessed on 4 August 2024).
55. Mubarok, F.; Armada, S.; Fagoaga, I.; Espallargas, N. Thermally Sprayed SiC Coatings for Offshore Wind Turbine Bearing Applications. *JTTEE5* **2013**, *22*, 156–163. [[CrossRef](#)]

56. Alonso, F.; Fagoaga, I.; Oregui, P. Erosion protection of carbon—Epoxy composites by plasma-sprayed coatings. *Surf. Coat. Technol.* **1991**, *49*, 482–488. [CrossRef]
57. Parco, M.; Zhao, L.; Zwick, J.; Bobzin, K.; Lugscheider, E. Investigation of HVOF spraying on magnesium alloys. *Surf. Coat. Technol.* **2006**, *201*, 3269–3274. [CrossRef]
58. Available online: <https://www.tecnalia.com/konbus-sistema-de-proyeccion-termica> (accessed on 4 August 2024).
59. Boualem, N.; Raid, A.; Ghaffor, M.A.; Tlemcani, A.; Derrar, M. Behavior of thermally sprayed WC-Co layers on 5086 aluminum alloy and 304 L stainless steel. *Key Eng. Mater.* **2013**, *550*, 41–47. [CrossRef]
60. Timelli, G.; Fabrizi, A.; Vezzù, S.; De Mori, A. Design of Wear-Resistant Diecast AlSi₉Cu₃(Fe) Alloys for High-Temperature Components. *Metals* **2020**, *10*, 55. [CrossRef]
61. Ghazali, M.J.; Rainfoth, W.M.; Omar, M.Z. A comparative study of mechanically mixed layers (MMLs) characteristics of commercial aluminium alloys sliding against alumina and steel sliders. *J. Mater. Process. Technol.* **2008**, *201*, 662–668. [CrossRef]
62. Ghazali, M.J.; Rainforth, W.M.; Jones, H. The wear of wrought aluminium alloys under dry sliding conditions. *Tribol. Int.* **2007**, *40*, 160–169. [CrossRef]
63. Torres, A.; Hernández, A.; García, A.; Viesca, J.L.; González, R.; Hadfield, M. Use of optical profilometry in the ASTM D4172 standard. *Wear* **2011**, *271*, 2963–2967. [CrossRef]
64. Pawlus, P.; Dzierwa, A. Wear Analysis of Discs and Balls on a Micro-Scale. *Teh. Vjesn.* **2018**, *25*, 299–305. [CrossRef]
65. Park, K.; Chang, B.Y.; Hwang, S. Correlation between Tafel Analysis and Electrochemical Impedance Spectroscopy by Prediction of Amperometric Response from EIS. *ACS Omega* **2019**, *4*, 19307–19313. [CrossRef]
66. Berger, L.M. Application of hardmetals as thermal spray coatings. *IJRMHM* **2015**, *49*, 350–364. [CrossRef]
67. Vignesh, S.; Shanmugam, K.; Balasubramanian, V.; Sridhar, K. Identifying the optimal HVOF spray parameters to attain minimum porosity and maximum hardness in iron based amorphous metallic coatings. *Def. Technol.* **2017**, *13*, 101–110. [CrossRef]
68. Mondal, C.; Mukhopadhyay, A.K. On the nature of T(Al₂Mg₃Zn₃) and S(Al₂CuMg) phases present in as-cast and annealed 7055 aluminum alloy. *Mater. Sci. Eng. A* **2005**, *391*, 367–376. [CrossRef]
69. Li, L.; Zheng, Y.; Chen, Y.; Feng, J.; Li, C.; Chen, L.; Zuo, L.; Zhang, Y. Study on Microstructure Distribution of Al-Cu-Mg Alloy in Squeeze Casting Process. *J. Phys. Conf. Ser. J. Phys. Conf. Ser.* **2022**, *2338*, 012038. [CrossRef]
70. Carranza, J.C.; Casas, B.Y.; Lopez, I.A.; Figueroa, I.A.; Gonzalez, G.; Hernandez, O.; Bejar, L.; Aguilar, C. Fractal and Conventional Analysis of Cu Content Effect on the Microstructure of Al-Si-Cu-Mg Alloys. *Mater. Res.* **2020**, *23*, e20190666. [CrossRef]
71. Kim, D.; Kwon, H. Interdiffusion and Intermetallic Compounds at Al/Cu Interfaces in Al-50vol.%Cu Composite Prepared by Solid-State Sintering. *Materials* **2021**, *14*, 4307. [CrossRef] [PubMed]
72. Belov, N.A.; Avksenteva, N.N. Quantitative analysis of the Al–Cu–Mg–Mn–Si phase diagram as applied to commercial aluminum alloys of series 2xxx. *Met. Sci. Heat Treat.* **2013**, *55*, 358–363. [CrossRef]
73. Kuang, R.; Yang, H.; Zheng, S.; Li, M.; Wang, H.; Duan, Y.; Yue, C.; Yang, C. The evolution mechanism of the second phase during homogenization of Al-Zn-Mg-Cu aluminum alloy. *Mater. Des.* **2023**, *235*, 112395.
74. Zhang, M.; Tian, Y.; Zheng, X.; Zhang, Y.; Chen, L.; Wang, J. Research Progress on Multi-Component Alloying and Heat Treatment of High Strength and Toughness Al–Si–Cu–Mg Cast Aluminum Alloys. *Materials* **2023**, *16*, 1065. [CrossRef] [PubMed]
75. Camara, A. HVFO y APS. Available online: <https://es.scribd.com/document/424202926/HVOF-y-APS> (accessed on 4 August 2024).
76. Bhaskaran, R.; Supekar, R.; Morteza, S.; Wang, W.; Zou, Y.; McDonald, A.; Mostaghimi, J.; Stoyanov, P. High-Entropy Alloy Coatings Deposited by Thermal Spraying: A Review of Strengthening Mechanisms, Performance Assessments and Perspectives on Future Applications. *Metals* **2023**, *13*, 579. [CrossRef]
77. Habibm, K.A.; Canom, D.L.; Serrano-Miram, J.; Rayon, E.; Dosta, R.S. Impact of Microstructure on Remelting Parameters and Mechanical Behavior of Thermally Sprayed NiCrBSi Coating. *J. Therm. Spray Technol.* **2024**, *33*, 290–307. [CrossRef]
78. Sobolev, V.V.; Guilemany, J.M. Investigation of Coating Porosity Formation during High Velocity Oxy-Fuel (HVOF) Spraying. *Mater. Lett.* **1994**, *18*, 304–308. [CrossRef]
79. Wen, K.; Yan, H.; Yan, L.; Liu, H.; Xiao, W.; Li, Y.; Gao, G.; Liu, R.; Ren, W. Evolution of S(Al₂CuMg) Phase During Fabrication Process and its Influence on Mechanical Property in a Commercial Al-6.5Zn-2.4Mg-2.2Cu Alloy. In *Advances in Machinery, Materials Science and Engineering Application IX*; IOS Press: Amsterdam, The Netherlands, 2023; pp. 155–165. [CrossRef]
80. Kralik, R.; Battosova, L.; Kihoulou, B.; Preilser, D.; Cieslar, M. High-Temperature Phase Transformations in Al-Li-Cu-Mg-Zr-Sc Alloy Studied via In Situ Electron Microscopy. *Crystals* **2024**, *14*, 136. [CrossRef]
81. Zhang, J.; Huang, Y.N.; Mao, C.; Peng, P. Structural, elastic, and electronic properties of θ (Al₂Cu) and S (Al₂CuMg) strengthening precipitates in Al–Cu–Mg series alloys: First-principles calculations. *Solid State Commun.* **2012**, *152*, 2100–2104. [CrossRef]
82. Al-Qutub, A.M.; Khalli, A.; Saheb, N.; Hakeem, A.S. Wear and friction behavior of Al6061 alloy reinforced with carbon nanotubes. *Wear* **2012**, *297*, 752–761. [CrossRef]
83. Rapoport, L.; Moshkovich, A.; Perfilyev, V.; Lapsker, I.; Kugler, M.; Kailer, A.; Renz, A.; Hollstein, T. High temperature friction behavior of CrVxN coatings. *Surf. Coat. Technol.* **2014**, *238*, 207–215. [CrossRef]
84. Joseph, J.; Haghdadi, N.; Shamlaye, K.; Hodgson, P.D.; Barnett, M.; Fabijanic, D. The sliding wear behaviour of CoCrFeMnNi and AlxCoCrFeNi high entropy alloys at elevated temperatures. *Wear* **2019**, *428–429*, 32–44. [CrossRef]
85. Wu, J.M.; Lin, S.J.; Yeh, J.W.; Chen, S.K.; Huang, Y.S.; Chen, H.C. Adhesive wear behavior of AlxCoCrCuFeNi high-entropy alloys as a function of aluminum content. *Wear* **2006**, *261*, 53–519. [CrossRef]

86. Michalak, M.; Sokolowski, P.; Szala, M.; Walczak, M.; Latka, L.; Toma, F.L.; Bjorklund, S. Wear Behavior Analysis of Al₂O₃ Coatings Manufactured by APS and HVOF Spraying Processes Using Powder and Suspension Feedstocks. *Coatings* **2021**, *11*, 879. [CrossRef]
87. Shyan, J.; Lin, C.; Kuen, Y.; Huang, E.W.; Fu, K.; Lee, S. The combination of rolling-and-T6-treatments with Al₂O₃-reinforcing-particles effect on A6061 metal-matrix composites. *Dep. Mater. Sci. Eng.* **2016**, *230*, 233–239. [CrossRef]
88. Elmadagli, M.; Perry, T.; Alpas, A.T. A parametric study of the relationship between microstructure and wear resistance of Al–Si alloy. *Wear* **2007**, *262*, 79–92. [CrossRef]
89. Zhang, J.; Alpas, A.T. Transition between mild and severe wear in aluminium alloys. *Acta Mater.* **1997**, *45*, 513–528. [CrossRef]
90. Li, H.; Jiao, L.; Xu, R.; Li, F.; Lu, S.B.; Qiao, Y.P.; Li, C.Y. Surface Wear Behavior and Friction and Wear Mechanism Studies of A356/3 wt.% Al₃Zr Composites. *J. Mater. Eng. Perform.* **2021**, *30*, 3892–3902. [CrossRef]
91. Silvello, A.; Torres, E.; Rua, E.; Garcia, I. Microstructural, Mechanical and Wear Properties of Atmospheric Plasma-Sprayed and High-Velocity Oxy-Fuel AlCoCrFeNi Equiatomic High-Entropy Alloys (HEAs) Coatings. *J. Therm. Spray Technol.* **2023**, *32*, 425–442. [CrossRef]
92. Khana, V.K. Adhesion–delamination phenomena at the surfaces and interfaces in microelectronics and MEMS structures and packaged devices. *J. Phys. D* **2011**, *44*, 034004. [CrossRef]
93. Olea-Mejia, O.; Brostow, W.; Buchman, E. Wear Resistance and Wear Mechanisms in Polymer + Metal Composites. *J. Nanosci. Nanotechnol.* **2010**, *10*, 8524–8530. [CrossRef] [PubMed]
94. Mora, J.; García, P.; Muelas, R.; Agüero, A. Hard Quasicrystalline Coatings Deposited by HVOF Thermal Spray to Reduce Ice Accretion in Aero-Structures Components. *Coatings* **2020**, *10*, 290. [CrossRef]
95. Reddy, S.; Kaliveeran, V. Wear of Dry Sliding Al 6061-T6 Alloy Under Different Loading Conditions. *IJSEIMS* **2022**, *10*, 1–12. [CrossRef]
96. Chang, Y.P.; Liu, C.T.; Chu, L.M.; Chou, H.M. Wear mechanisms of aluminum 5083/6061/7075 with and without T6 treatment. *Adv. Mech. Eng.* **2023**, *15*, 1–12. [CrossRef]
97. Antler, M. Sliding Wear of Metallic Contacts. *IEEE Trans. Compon. Hybrids Manuf. Technol.* **1981**, *4*, 15–29. [CrossRef]
98. Pan, C.T.; Wu, C.N.; Mao, S.W.; Wang, S.Y.; Ju, S.P.; Wu, J.D.; Yen, C.K.; Chen, W.F. Adhesion–delamination phenomena at the interfaces of the dielectric layer. *Results Phys.* **2020**, *18*, 103249. [CrossRef]
99. Siopis, M.J.; Cowan, R.S. High Velocity Wear: Experiments and Modeling. In Proceedings of the 17th International Symposium on Electromagnetic Launch Technology, La Jolla, CA, USA, 7–11 July 2014. [CrossRef]
100. Electrical Conductivity and Resistivity for Aluminum and Aluminum Alloys. Available online: https://www.nde-ed.org/NDETechniques/EddyCurrent/ET_Tables/standardmethods.xhtml (accessed on 4 August 2024).
101. Voyer, J. Flexible and Conducting Metal-Fabric Composites Using the Flame Spray Process for the Production of Li-Ion Batteries. *J. Therm. Spray Technol.* **2013**, *22*, 699–709. [CrossRef]
102. Kim, J.K.; Kee, S.H.; Futralan, C.M.; Yee, J.J. Corrosion Monitoring of Reinforced Steel Embedded in Cement Mortar under Wet-And-Dry Cycles by Electrochemical Impedance Spectroscopy. *Sensors* **2020**, *20*, 199. [CrossRef]
103. Chen, Y.; Yin, Z.; Yan, H.; Zhou, G.H.; Wu, X.Q.; Hu, Z. Effect of Samarium on the Microstructure and Corrosion Resistance of AZ91 Magnesium Alloy Treated by Ultrasonic Vibration. *Materials* **2018**, *11*, 2331. [CrossRef]
104. Lu, Q.; Zhao, Y.; Wang, Q.; Li, D. Investigation on the Corrosion Resistance of 3003 Aluminum Alloy in Acidic Salt Spray under Different Processing States. *Metals* **2024**, *14*, 196. [CrossRef]
105. Kuchariková, L.; Liptáková, T.; Tillová, E.; Kajánek, D.; Schmidová, E. Role of Chemical Composition in Corrosion of Aluminum Alloys. *Metals* **2018**, *8*, 581. [CrossRef]
106. Abbass, M.; Hassan, K.; Alwan, A.S. Study of Corrosion Resistance of Aluminum Alloy 6061/SiC Composites in 3.5% NaCl Solution. *IJMMM* **2015**, *3*, 31–35. [CrossRef]
107. Ananda, H.C.; Kumar, S. Influence Of TiC Particulate Reinforcement On The Corrosion Behaviour of Al 6061 Metal Matrix Composites. *Adv. Mater. Lett.* **2015**, *6*, 633–640. [CrossRef]
108. Ramos, O.J.; Escobar, R.F.; Arellano, J.H.; Gomez, J.F.; Xia, D.H. Corrosion analysis in the Al6061-T6 alloy exposed to anhydrous ethanol-gasoline blends using the Stockwell transform and the Shannon energy. *J. Alloys Compd.* **2022**, *902*, 163802. [CrossRef]
109. Berlanga, C.; Biezma, M.V.; Rivero, P.J. Corrosion of Cast Aluminum Alloys: A Review. *Metals* **2020**, *10*, 1384. [CrossRef]
110. Voncina, M.; Mocnik, N.; Nagode, A.; Stoic, A.; Bizjak, M. Dependence of mechanical properties on Cu content in AlSi₉Cu₃(Fe) alloy. *Teh. Vjesn.-Tech. Gaz.* **2017**, *24*, 229. [CrossRef]
111. Pérez, A. Estudio del Comportamiento Frente a Corrosión de una Nueva Aleación Secundaria AlSi₁₀MnMg (Fe). Master’s Thesis, Universidad Pública de Navarra, Navarra, Spain, 2017.
112. Zbontar, M.; Petric, M.; Mrvar, P. The Influence of Cooling Rate on Microstructure and Mechanical Properties of AlSi₉Cu₃. *Metals* **2021**, *11*, 186. [CrossRef]
113. Fauchais, P.; Montavon, G.; Bertrand, G. From Powders to Thermally Sprayed Coatings. *JTTEE5* **2009**, *19*, 56–80. [CrossRef]
114. Analysis of Controlled Air Cooling for Castings by Experiment and Simulation. Available online: <https://www.foundry-planet.com/d/analysis-of-controlled-air-cooling-for-castings-by-experiment-and-simulation/> (accessed on 4 August 2024).
115. Lim, L.; Lim, D.; Fengm, J.; Zhangm, Y.; Kangm, Y. Effect of Cooling Rates on the Microstructure and Mechanical Property of La Modified Al7SiMg Alloys Processed by Gravity Die Casting and Semi-Solid Die Casting. *Metals* **2020**, *10*, 549. [CrossRef]

116. Lombardim, A.N.; Castelettim, L.C.; Tottenm, G.E. Thermal Spray Technologies: An Overview. In *Encyclopedia of Tribology*; Springer: Boston, MA, USA, 2013; pp. 3607–3617. [[CrossRef](#)]
117. Zhu, X.; Dong, X.; Blake, P.; Ji, S.; Strength Improvement in High Pressure Die-Cast Al-Si-Cu Alloys by Synergistic Strengthening of Q-Al₅Cu₂Mg₈Si₆ and θ -Al₂Cu Phases. Brunel University Research Archive. Available online: <https://bura.brunel.ac.uk/bitstream/2438/22434/1/FullText.pdf> (accessed on 4 August 2024).
118. Khangholi, S.N.; Javidani, M.; Maltais, A.; Chen, X.G. Effect of Ag and Cu addition on the strength and electrical conductivity of Al-Mg-Si alloys using conventional and modified thermomechanical treatments. *J. Alloys Compd.* **2022**, *914*, 165242. [[CrossRef](#)]
119. Xu, S.; Lin, B.; Jiang, Y.; He, X.; Fan, Z.; Xiao, H.; Fu, Z. Simultaneously improving mechanical properties and electrical conductivity of Al-1.9Mn alloys with different Mg and Si addition. *J. Alloys Compd.* **2024**, *999*, 175072. [[CrossRef](#)]
120. Sunde, J.K.; Marioara, C.D.; Wenner, S.; Holmestad, R. On the microstructural origins of improvements in conductivity by heavy deformation and ageing of Al-Mg-Si alloy 6101. *Mater. Charact.* **2021**, *176*, 111073. [[CrossRef](#)]
121. Vandersluis, E.; Ravindran, C.R. Effects of solution heat treatment time on the as-quenched microstructure, hardness and electrical conductivity of B319 aluminum alloy. *J. Alloys Compd.* **2020**, *838*, 155577. [[CrossRef](#)]
122. Murashin, M.; Medvedec, A.; Kazykhanov, V.; Krokhin, A.; Raab, G.; Enikeev, N.; Valiev, R.Z. Enhanced Mechanical Properties and Electrical Conductivity in Ultrafine-Grained Al 6101 Alloy Processed via ECAP-Conform. *Metals* **2015**, *5*, 2148–2164. [[CrossRef](#)]
123. Nikzad, S.; Javidani, M.; Maltais, A.; Chen, X.G. Review on recent progress in Al-Mg-Si 6xxx conductor alloys. *J. Mater. Res.* **2022**, *37*, 670–691. [[CrossRef](#)]

Disclaimer/Publisher’s Note: The statements, opinions and data contained in all publications are solely those of the individual author(s) and contributor(s) and not of MDPI and/or the editor(s). MDPI and/or the editor(s) disclaim responsibility for any injury to people or property resulting from any ideas, methods, instructions or products referred to in the content.